



GRB 110530A: PECULIAR BROAD BUMP AND DELAYED PLATEAU IN EARLY OPTICAL AFTERGLOWS

SHU-QING ZHONG^{1,2}, LI-PING XIN³, EN-WEI LIANG^{1,2,3,4}, JIAN-YAN WEI³, YUJI URATA^{5,6}, KUI-YUN HUANG⁷, YU-LEI QIU³,
CAN-MIN DENG^{1,2}, YUAN-ZHU WANG⁴, AND JIN-SONG DENG³

¹ GXU-NAOC Center for Astrophysics and Space Sciences, Department of Physics, Guangxi University, Nanning 530004, China; lew@gxu.edu.cn

² Guangxi Key Laboratory for the Relativistic Astrophysics, Nanning 530004, China

³ Key Laboratory of Space Astronomy and Technology, National Astronomical Observatories, Chinese Academy of Sciences, Beijing 100012, China; xlp@bao.ac.cn

⁴ Purple Mountain Observatory, Chinese Academy of Sciences, Nanjing 210008, China

⁵ Institute of Astronomy, National Central University, Chung-Li 32054, Taiwan

⁶ Academia Sinica Institute of Astronomy and Astrophysics, Taipei 106, Taiwan

⁷ Department of Mathematics and Science, National Taiwan Normal University, Lin-kou District, New Taipei City 24449, Taiwan

Received 2016 February 5; revised 2016 July 26; accepted 2016 July 26; published 2016 October 20

ABSTRACT

We report our very early optical observations of GRB 110530A and investigate its jet properties together with its X-ray afterglow data. A peculiar broad onset bump followed by a plateau is observed in its early *R* band afterglow light curve. The optical data in the other bands and the X-ray data are well consistent with the temporal feature of the *R* band light curve. Our joint spectral fits of the optical and X-ray data show that they are in the same regime, with a photon index of ~ 1.70 . The optical and X-ray afterglow light curves are well fitted with the standard external shock model by considering a delayed energy injection component. Based on our modeling results, we find that the radiative efficiency of the gamma-ray burst jet is $\sim 1\%$ and the magnetization parameter of the afterglow jet is < 0.04 with a derived extremely low ϵ_B (the ratio of shock energy to the magnetic field) of $(1.64 \pm 0.25) \times 10^{-6}$. These results indicate that the jet may be matter dominated. A discussion on delayed energy injection from the accretion of the late fall-back material of its pre-supernova star is also presented.

Key words: gamma-ray burst; general

1. INTRODUCTION

It is generally believed that cosmic gamma-ray bursts (GRBs) are from ultra-relativistic jets powered by newly born black holes or pulsars during collapses of massive stars or mergers of compact stars (e.g., Colgate 1974; Paczynski 1986; Eichler et al. 1989; Narayan et al. 1992; Woosley 1993; MacFadyen & Woosley 1999; Zhang et al. 2003; see reviews by Mészáros 2002, 2006; Piran 2004; Zhang & Mészáros 2004; Woosley & Bloom 2006; Kumar & Zhang 2015). Their prompt gamma-ray emission may be from internal shocks in an erratic, unsteady, relativistic fireball (e.g., Rees & Meszaros 1992; Meszaros & Rees 1993; Rees & Meszaros 1994), a dissipative photosphere (e.g., Giannios 2008; Beloborodov 2010; Ioka 2010; Vurm et al. 2011), or a Poynting-flux-dominated outflow (Zhang & Yan 2011 and references therein). The broad band observations with the *Fermi* mission sharpen the debate on the radiation mechanisms and the composition of GRB jets (e.g., Abdo et al. 2009; Zhang & Pe'er 2009; 2011, 2013; Lyu et al. 2014).

Long-lived afterglows in the X-ray, optical, and radio bands following the prompt gamma-rays were discovered in the *BeppoSAX* mission era (van Paradijs et al. 2000 and references therein). They are well explained by the synchrotron emission from external shocks when GRB fireballs propagate into the circumburst medium (e.g., Mészáros & Rees 1997; Sari et al. 1998; Gao et al. 2013). Afterglow observations were revolutionized by the *Swift* mission thanks to the prompt slewing and precise localizing capacities of its X-ray telescope (XRT) (Gehrels et al. 2004; Burrows et al. 2005a). The number of GRBs that have optical and X-ray afterglow detections is rapidly increasing and the sample of well-sampled light curves is also growing quickly (Gehrels et al. 2009; Kann et al. 2010). Excluding the tail emission of the prompt gamma-rays and erratic flares from the canonical XRT light curves (Nousek

et al. 2006; Zhang et al. 2006), the X-ray afterglow light curves are generally consistent with the predictions of the external shock model when an extra energy injection is added (Zhang et al. 2006; Liang et al. 2007). Statistical analysis of optical afterglow light curves observed from 1997 February to 2011 November shows that about 1/3 of the optical afterglow light curves well agree with the prediction of the external shock model in the thin shell case, and another 1/3 may require an extra energy injection to the external shocked medium (Li et al. 2012; Liang et al. 2013). An extensive analysis of X-ray and optical afterglow data by Wang et al. (2015) shows that the standard external shock models are good for explaining the data by elaborately considering various effects, such as long-lasting reverse shock, structured jets, and the circumburst medium's density profile.

Well-sampled multi-wavelength light curves in broad temporal coverage from very early to late epochs are valuable for modeling the light curves and revealing the properties of GRB jets and even the GRB central engines as well as the progenitors (e.g., Xin et al. 2016). This paper reports our very early optical observations for GRB 110530A and detailed modeling for the optical and X-ray afterglow light curves. Observations and data reductions are reported in Section 2. We present joint temporal and spectral analysis for the optical and X-ray afterglow data in Section 3, and present our modeling results in Section 4. A discussion on the possible implications for the jet composition and progenitor star is presented in Section 5. Conclusions are presented in Section 6. The notation $Q_n = Q/10^n$ in cgs is adopted throughout.

2. OBSERVATIONS AND DATA REDUCTION

The XRT and UV-Optical Telescope (UVOT) on board *Swift* began observing the X-ray and optical afterglows of GRB 110530A at 446 and 438 s, respectively, after the *Swift* Burst

Alert Telescope (BAT) trigger (D’Avanzo et al. 2011a, 2011b). Our optical follow-up observations began much earlier than the first detections of the XRT and UVOT (Marshall & D’Avanzo 2011). The 0.8 m Tsinghua University–National Astronomical Observatory of China Telescope (TNT) at Xinglong Observatory⁸ promptly slewed to the burst position 133 s after the *Swift*/BAT trigger, and the optical counterpart was clearly detected in all images in the *white* (*W*) and *R* bands. The early optical afterglows of GRB 110530A were also observed with the AZT-33IK telescope of the Sayan Observatory (Mondy) and a well-sampled light curve was obtained (Volnova et al. 2011). Our observations with the Lulin One-Meter Telescope (LOT) in Taiwan started at about 30 minutes after the burst, and the optical counterpart was also clearly detected in the *g*, *r*, and *i* bands. The optical counterpart was also detected with the 2.5 m Nordic Optical Telescope (NOT) at Roque de los Muchachos Observatory (La Palma, Spain) at 6.8 hr after the burst. It faded down to $R \sim 21.3$ mag (De Cia et al. 2011). Spectroscopic observations with the NOT do not show any evident absorption lines, and a limit of the redshift $z < 2.7$ is placed by the non-detection of Lyman alpha absorption in the spectra (De Cia et al. 2011). We assume that $z = 1$ for our analysis.

We process our optical data by following the standard routine in the IRAF package.⁹ Point spread function photometry was applied with the DAOPHOT tool in the IRAF package to obtain the instrumental magnitudes. For the *white* band data, we simply take them as *R* band data (Xin et al. 2010). All TNT optical data were calibrated by USNO B1.0 R2 mag with 11 nearby reference stars. The data observed with the LOT were calibrated with the transformation of Jordi et al. (2006)¹⁰ with USNO B1.0 mag. Our optical observations are reported in Table 1, and the optical afterglow light curves are shown in Figure 1. The reference stars for calibration are presented in Table 2.

The *Swift*/XRT light curve and spectrum are obtained from the UK Swift Science Data Centre at the University of Leicester (Evans et al. 2009).¹¹ The XRT light curve with 30 counts per bin is also shown in Figure 1.

The duration of prompt emission in the BAT band is $T_{90} = 19.6$ s. We extract the prompt gamma-ray spectrum following the standard BAT data processing routine. It is well known that the GRB spectrum in the keV–MeV band is empirically fitted by the Band function with typical photon indices $\Gamma_1 = -1$ and $\Gamma_2 = -2.3$ breaking at E_b (Band et al. 1993; Preece et al. 2000). The peak energy of the νf_ν spectrum is given by $E_p = (1 + \Gamma_1)$ if $\Gamma_2 < -2$. The E_p value may vary from tens to thousands of keVs among GRBs. Since the BAT energy band is only 15–150 keV, the GRB spectrum observed with the BAT is usually adequately fitted with a single power-law, and an empirical relation between E_p and Γ_γ is proposed, i.e., $\log E_p = (2.76 \pm 0.07) - (3.61 \pm 0.26) \log \Gamma$ (Zhang et al. 2007a). Fitting the BAT spectrum of GRB 110530A with a single power-law, we get

Table 1
Optical Afterglow Photometry Log of GRB 110530A

T-T0(mid, second)	Exposure (s)	Mag ^a	σ^a	Filter	Telescope
144	20	19.24	0.34	W	TNT
167	20	19.39	0.24	W	TNT
190	20	18.99	0.22	W	TNT
213	20	19.01	0.12	W	TNT
235	20	18.86	0.18	W	TNT
258	20	18.59	0.14	W	TNT
281	20	18.63	0.14	W	TNT
303	20	18.54	0.14	W	TNT
326	20	18.56	0.14	W	TNT
349	20	18.54	0.10	W	TNT
372	20	18.60	0.12	W	TNT
394	20	18.54	0.15	W	TNT
417	20	18.66	0.16	W	TNT
440	20	18.53	0.13	W	TNT
463	20	18.27	0.12	W	TNT
485	20	18.41	0.11	W	TNT
508	20	18.43	0.14	W	TNT
531	20	18.36	0.13	W	TNT
553	20	18.48	0.12	W	TNT
605	60	18.62	0.09	R	TNT
684	60	18.47	0.08	R	TNT
763	60	18.45	0.07	R	TNT
841	60	18.49	0.10	R	TNT
919	60	18.37	0.08	R	TNT
998	60	18.60	0.10	R	TNT
1076	60	18.64	0.12	R	TNT
1155	60	18.49	0.08	R	TNT
1233	60	18.62	0.11	R	TNT
1312	60	18.67	0.12	R	TNT
1390	60	18.76	0.13	R	TNT
1469	60	18.83	0.11	R	TNT
1547	60	19.17	0.18	R	TNT
1625	60	18.92	0.14	R	TNT
1704	60	19.08	0.14	R	TNT
1782	60	19.01	0.16	R	TNT
1861	60	19.03	0.14	R	TNT
1939	60	19.27	0.23	R	TNT
2018	60	19.17	0.17	R	TNT
2096	60	19.53	0.24	R	TNT
2297	300	19.33	0.08	R	TNT
2614	300	19.46	0.08	R	TNT
2932	300	19.40	0.07	R	TNT
3250	300	19.44	0.08	R	TNT
3567	300	19.36	0.07	R	TNT
3885	300	19.44	0.09	R	TNT
4203	300	19.53	0.09	R	TNT
4520	300	19.65	0.09	R	TNT
4838	300	19.50	0.08	R	TNT
5156	300	19.84	0.10	R	TNT
5473	300	19.70	0.10	R	TNT
6109	300	19.68	0.09	R	TNT
6427	300	19.82	0.10	R	TNT
6744	300	19.73	0.10	R	TNT
7062	300	20.04	0.11	R	TNT
7380	300	20.13	0.12	R	TNT
7697	300	20.27	0.14	R	TNT
8015	300	20.26	0.14	R	TNT
8333	300	20.19	0.13	R	TNT
8650	300	20.23	0.15	R	TNT
8968	300	20.34	0.15	R	TNT
9286	300	20.09	0.12	R	TNT
9604	300	20.11	0.12	R	TNT
10371	600	20.49	0.10	R	TNT
10557	300	20.30	0.14	R	TNT

⁸ The TNT is a 0.8 m telescope run by a custom-designed automation system for GRB follow-up observations at Xinglong Observatory. It is equipped with a PI 1300 × 1340 CCD and filters in the standard Johnson–Bessel system (Zheng et al. 2008).

⁹ IRAF is distributed by NOAO, which is operated by AURA, Inc., under a cooperative agreement with the NSF.

¹⁰ <http://classic.sdss.org/dr6/algorithms/sdssUBVRITransform.html#Jordi2006>

¹¹ <http://www.swift.ac.uk/results.shtml>

Table 1
(Continued)

T-T0(mid, second)	Exposure (s)	Mag ^a	σ^a	Filter	Telescope
11624	900	20.51	0.10	R	TNT
13177	1500	20.66	0.09	R	TNT
14166	900	21.00	0.20	R	TNT
15719	1500	21.17	0.46	R	TNT
79442	3000	>21.91	...	R	TNT
1835	300	19.59	0.14	g	LOT
2814	300	19.82	0.17	g	LOT
3792	300	19.78	0.24	g	LOT
4771	300	19.92	0.15	g	LOT
5749	300	20.11	0.17	g	LOT
6727	300	20.31	0.16	g	LOT
2486	300	19.11	0.15	i	LOT
3465	300	19.05	0.19	i	LOT
4443	300	19.14	0.17	i	LOT
5421	300	19.26	0.17	i	LOT
6399	300	19.24	0.21	i	LOT
7377	300	19.25	0.18	i	LOT
1381	300	19.02	0.12	r	LOT
2161	300	19.59	0.14	r	LOT
3139	300	19.52	0.14	r	LOT
4118	300	19.75	0.21	r	LOT
5096	300	19.87	0.15	r	LOT
6074	300	19.91	0.14	r	LOT
7052	300	20.18	0.16	r	LOT
512	74	20.30	0.14	white	UVOT
939	74	20.32	0.14	white	UVOT
7748	546	21.48	0.20	white	UVOT
13369	707	22.07	0.25	white	UVOT
17892	1976	>22.88	...	white	UVOT
21569	1230	>22.83	...	white	UVOT

Note.

^a Not corrected for Galactic foreground reddening. The reference time T_0 is the *Swift* BAT burst trigger time. “T–T0” is the middle time in seconds for each datum. “Exposure” is the exposure time for each datum in seconds, and “ σ ” indicates the uncertainty of the magnitude.

$\Gamma_\gamma = 2.04 \pm 0.21$, and its fluence in the BAT energy band is 3.3×10^{-7} erg cm⁻² in this spectral model. With the empirical relation between E_p and Γ_γ , we have $E_p \sim 45$ keV. Correcting $E_{\gamma, \text{iso}}$ in the BAT band to the 1–10⁴ keV band with the spectral parameters $\Gamma_1 = -1$, $\Gamma_2 = -2.3$, and $E_p = 45$ keV, we obtain $E_{\gamma, \text{iso}}^c = 1.92 \times 10^{51}$ erg, assuming $z = 1$. With the spectral parameters, we also obtain the peak luminosity in the 1–10⁴ keV band as $L_{\gamma, \text{iso}}^c = (2.81 \pm 0.71) \times 10^{50}$ erg s⁻¹.

3. DATA ANALYSIS

As shown in Figure 1, a well-sampled light curve in the *R* band is observed with the TNT. We empirically fit the light curve with a multiple broken power-law model. Each broken power-law function is read as

$$F = F_0 \left[\left(\frac{t}{t_b} \right)^{\omega\alpha_1} + \left(\frac{t}{t_b} \right)^{\omega\alpha_2} \right]^{1/\omega}, \quad (1)$$

where t_b is the break time; α_1 and α_2 are the decay indices before and after the break, respectively; and ω describes the sharpness of the break. Our fit yields five phases, as shown on the right panel of Figure 1. The *R* band light curve smoothly onsets with a slope of 2.6 ± 0.4 (Phase I) and peaks at

275 ± 22 s. The flux remains almost constant from 275 to 1300 s (the first plateau, Phase II) and then decays with a power-law index of -1.2 (Phase III). Subsequently, the flux stays almost constant (the second plateau, Phase IV) and transits to a normal decay with a power-law of -1.2 again (Phase V). Flickering shows up at around $T_0 + 460$ and $T_0 + 1200$ s during the first optical plateau. Re-scaling the multi-band optical data and XRT data clearly shows that both other-wavelength optical data and X-ray data are well consistent with the temporal feature of the *R* band light curve; even the optical flickering feature also clearly shows up in the X-ray band. These results strongly indicate that the optical and X-ray afterglows are from the same emission component. Such a light curve shape has been seen before in other GRB afterglows, though with a less pronounced early plateau, such as in GRB 071025 (Perley et al. 2010), GRB 091024 (Virgili et al. 2013), and GRB 110213A (Cucchiara et al. 2011). An early rise–plateau–decay was also recently reported for GRB 141221A, although no second hump was observed (Bardho et al. 2016).

To investigate the spectral properties of the afterglow data, we extract the joint optical and X-ray spectra of the afterglows in five time intervals, i.e., 0.6–0.9 ks, 0.9–1.37 ks, 1.37–2.5 ks, 6–9 ks, and 9–14 ks. The X-ray data in each time interval are grouped with a criterion of 10 counts per bin. The selected time intervals are for Phases II–V and the late epoch of Phase V. Spectral analysis for Phase I could not be made since no X-ray data are available. The optical data are corrected by the extinction of our Galaxy: $A_g = 0.182$, $A_r = 0.126$, $A_R = 0.119$, and $A_i = 0.093$ at the burst direction (Schlegel et al. 1998). The equivalent hydrogen column density of our Galaxy is $N_H = 6.78 \times 10^{20}$ cm⁻². We use the Xspec package to analyze the spectral data. The extinction laws of the host galaxy are taken as those of the Large Magellanic Cloud (LMC; $R_V = 3.16$) and Small Magellanic Cloud (SMC; $R_V = 2.93$). The N_H of the host galaxy is derived from the time-integrated X-ray afterglow spectrum. It is $N_H^{\text{host}} \sim 1.0 \times 10^{21}$ cm⁻², which is fixed at this value in our time-resolved spectral fits. Considering the hydrogen absorptions and extinctions of both our Galaxy and the host galaxy, we fit the spectra with a single power-law function. Our results are reported in Table 3 and shown in Figure 2. The derived photon indices range from 1.67 to 1.72. The extinction by the host galaxy is negligible for both the LMC and SMC extinction laws.¹²

4. MODELING THE OPTICAL AND X-RAY AFTERGLOW LIGHT CURVES

Our temporal and spectral analysis shows that the optical and X-ray afterglows are from the same emission component. The clear detection of the smooth onset feature in the early optical data is well consistent with the expectation of the standard external shock model in the thin shell case (Sari & Piran 1999; Liang et al. 2010, 2013). The observed first plateau seems to be shaped by the broadening of the onset bump with superimposed flares (or flickering), which may be due to fluctuations

¹² Note that the redshift of GRB 110530A is unknown and we have only an upper limit of $z < 2.7$ (De Cia et al. 2011). Our dust modelings may be insecure since the LMC and SMC extinction curves, especially the LMC dust curve, have features which become relevant in this redshift range.

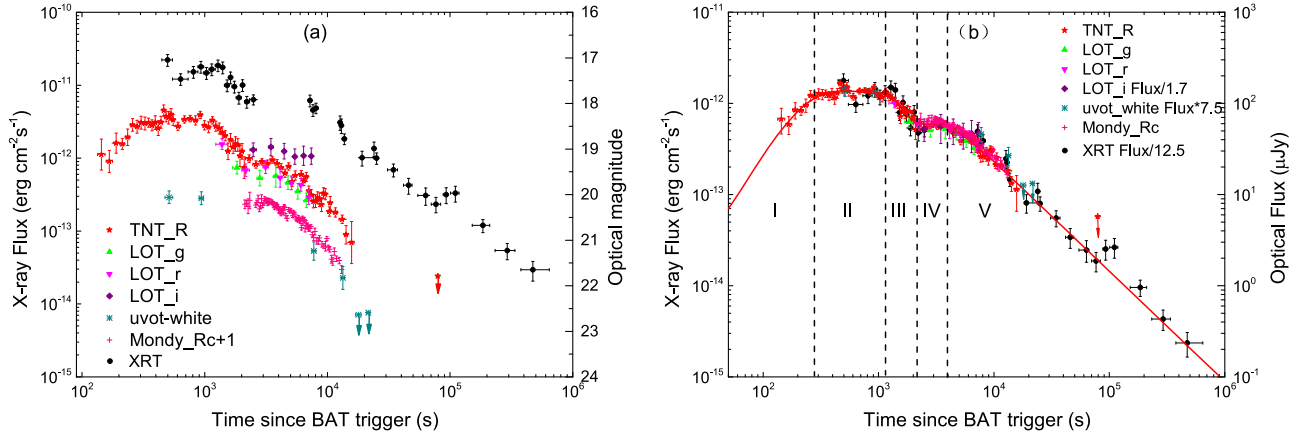


Figure 1. Observed optical and X-ray afterglow light curves of GRB 110530A (left panel) and our empirical fit with multiple smooth broken power-laws for the R band light curves (right panel). The optical data in the bands and the XRT data on the right panel are re-scaled in order to show the consistency of their temporal feature with the R band light curve. Phases identified from our empirical fit are also marked. Early optical afterglow data observed with the AZT-331K telescope of Sayan Observatory (Mondy), obtained from Volnova et al. (2011), are also illustrated for comparison.

Table 2
Reference Stars for Magnitude Calibration

R.A.	Decl.	Epoch	B_2	R_2	I
18:48:17.785	+61:55:56.69	J2000	18.63	17.07	16.08
18:48:15.583	+61:56:13.39	J2000	17.48	16.08	14.86
18:48:15.951	+61:56:25.06	J2000	18.41	17.23	17.02
18:48:10.257	+61:55:43.25	J2000	17.49	16.05	15.08
18:48:08.206	+61:55:40.41	J2000	17.09	16.88	16.30
18:48:05.743	+61:54:51.29	J2000	17.41	16.93	16.37
18:48:19.011	+61:54:43.98	J2000	15.15	14.03	13.20
18:48:23.664	+61:55:10.04	J2000	16.11	15.34	14.80
18:48:27.258	+61:55:12.79	J2000	16.17	15.36	14.30
18:48:26.344	+61:56:20.09	J2000	16.24	15.77	15.58
18:48:22.675	+61:56:37.35	J2000	16.49	16.10	15.47

Note. Reference stars for the calibration in this work. The B_2 , R_2 , and I -band magnitudes are extracted from the USNO B1.0 catalog.

Table 3
Spectral Analysis of the Optical and X-ray Afterglows in Selected Time Intervals

Interval(s)	Model(χ^2/dof)	PhoIndex(Γ)
0.6k–0.9k	LMC*PL(7.54/7 = 1.08)	1.70 ± 0.02
	SMC*PL(7.54/7 = 1.08)	1.70 ± 0.02
0.9k–1.37k	LMC*PL(15.79/13 = 1.214)	1.68 ± 0.13
	SMC*PL(15.79/13 = 1.215)	1.68 ± 0.13
1.37k–2.5k	LMC*PL(33.83/22 = 1.538)	1.72 ± 0.04
	SMC*PL(33.83/22 = 1.538)	1.72 ± 0.04
6k–9k	LMC*PL(31.58/11 = 2.871)	1.67 ± 0.02
	SMC*PL(31.59/11 = 2.872)	1.67 ± 0.02
9k–14k	LMC*PL(3.03/4 = 0.758)	1.72 ± 0.03
	SMC*PL(3.03/4 = 0.758)	1.72 ± 0.03

of the external shock region or due to flares from late internal shocks (e.g., Burrows et al. 2005b; Fan & Wei 2005; Dai et al. 2006; Liang et al. 2006; Zhang et al. 2006). We do not consider these erratic flares in our modeling. The second plateau from 2400 to 3000 s could be attributed to delayed energy injection to the afterglow jet. Therefore, we model the light curves with the standard afterglow models by considering the effect of late energy injection. We adopt the standard afterglow model by

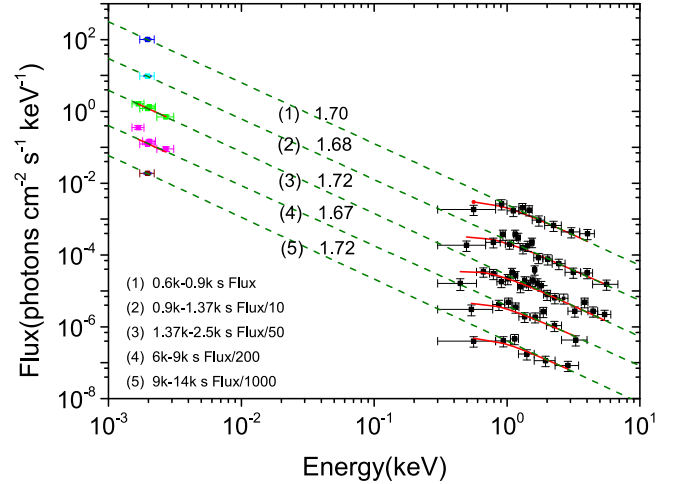


Figure 2. Joint spectral fits for the optical and X-ray afterglows with a single power-law function in the selected five time intervals. The olive dashed lines show the intrinsic power-law spectrum derived from the joint fits. The photon indices are also marked.

Sari et al. (1998) and Huang et al. (1999). We describe our model fitting strategy as follows:

1. Constraining the medium property and the power-law index of the radiating electrons with the closure relation of the forward shock model. With the decay slope and spectral index of the normal decay phase (Phase V), we find that the afterglows are radiated in the spectral regime of $\nu_m < \nu < \nu_c$. In this regime we have $p = 2\beta + 1$, where $\beta = \Gamma - 1$. We therefore obtain $p = 2.44 \pm 0.06$. We fix $p = 2.4$ in our analysis without considering the uncertainty of p . Note that the slope of the afterglow onset (Phase I) is $\alpha_1 = 2.6 \pm 0.4$, which well agrees with the expectation for a constant-density interstellar medium. The medium density in our fit is then set as a constant n .
2. Describing the energy injection as $L_{\text{in}} = L_0 t^q$ from the starting (t_s) to the ending (t_e) time in order to explain Phase IV.
3. Adopting the Markov chain Monte Carlo (MCMC) technique to search for the parameter set that can best represent the data. The parameters of our model

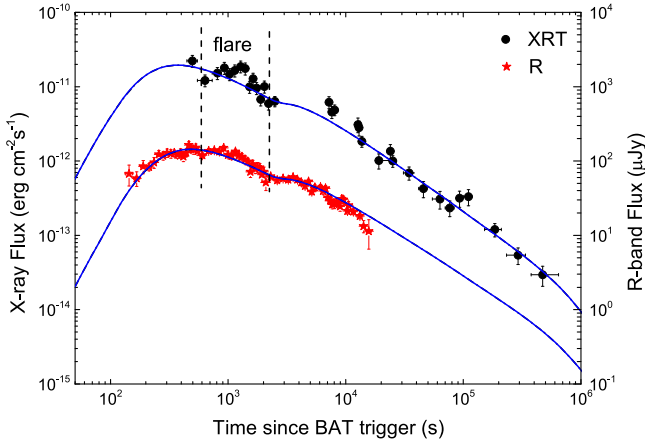


Figure 3. Fits to the optical and X-ray afterglow light curves using the standard external shock model by considering a delayed energy injection behaving as $L_{\text{in}} = L_0 t^q$. The model parameters derived from the MCMC technique are $\Gamma_0 = 91 \pm 8$, $\epsilon_e = 0.086 \pm 0.008$, $\epsilon_B = (1.64 \pm 0.25) \times 10^{-6}$, $n = 13.3 \pm 2.6 \text{ cm}^{-3}$, $E_{\text{K,iso}} = (2.28 \pm 0.27) \times 10^{53} \text{ erg}$, $t_s \sim 2400 \text{ s}$, $t_e = 2997 \pm 546 \text{ s}$, $L_0 = (4.0 \pm 2.5) \times 10^{50} \text{ erg s}^{-1}$, $q = -0.18_{-0.07}^{+0.05}$, and $\theta_j > 0.15 \text{ rad}$. The flare-like X-ray data at around 10^3 are not included in our fits.

include the initial Lorentz factor (Γ_0), the ratio of shock energy to the electron (ϵ_e), the ratio of shock energy to the magnetic field (ϵ_B), the medium density (n), the isotropic kinetic energy ($E_{\text{K,iso}}$), the jet opening angle (θ_j), and the parameters of the energy injection (L_0 , q , t_s , and t_e). They are set in the following ranges: $\Gamma_0 \in [50, 150]$, $\epsilon_e \in [0.01, 0.5]$, $\epsilon_B \in [10^{-7}, 10^{-4}]$, $n \in [0.1, 25]$, $E_{\text{K,iso}} \in [10^{51}, 10^{54}] \text{ erg}$, $\theta_j \in [0.01, 0.5] \text{ rad}$, $t_s \in [1000, 3000] \text{ s}$, $t_e \in [3000, 5000] \text{ s}$, $L_0 \in [10^{49}, 10^{52}] \text{ erg s}^{-1}$, and $q \in [-0.3, -0.1]$. We calculate χ^2 and measure the goodness of fit for each parameter set with a normalized probability $p_f \propto e^{-\chi^2/2}$. Note that the light curves are composed of some flares. With the MCMC technique we search for the parameter set that has the minimum χ^2 (and hence the largest p_f value). The uncertainty of a parameter in the best parameter set is evaluated by fixing the other parameters.

With this strategy, the best parameters and their uncertainty (1 σ confidence level) are $\Gamma_0 = 91 \pm 8$, $\epsilon_e = 0.086 \pm 0.008$, $\epsilon_B = (1.64 \pm 0.25) \times 10^{-6}$, $n = 13.3 \pm 2.6 \text{ cm}^{-3}$, $E_{\text{K,iso}} = (2.28 \pm 0.27) \times 10^{53} \text{ erg}$, $t_s \sim 2400 \text{ s}$, $t_e = 2997 \pm 546 \text{ s}$, $L_0 = (4.0 \pm 2.5) \times 10^{50} \text{ erg s}^{-1}$, and $q = -0.18_{-0.07}^{+0.05}$. The jet opening angle is poorly constrained, and we have $\theta_j > 0.15 \text{ rad}$. Figure 3 shows our best fit to the data with our model. The χ^2 of the fit is 1.605. The large χ^2 is due to flares/fluctuations in the optical and X-ray bands. The derived ϵ_e is generally consistent with previous results (Wijers & Galama 1999; Panaitescu & Kumar 2001; Yost et al. 2003; Liang et al. 2004), but ϵ_B is much lower than the typical value, i.e., 10^{-2} (e.g., Panaitescu & Kumar 2001). A further discussion on ϵ_B is presented in Section 5.1. The Γ_0 of GRB 110530A is at the lower end of the Γ_0 distribution for a sample of GRBs whose Γ_0 values are calculated with the deceleration

¹³ Some recent statistical analyses suggest a low ϵ_B , i.e., $[10^{-6}, 10^{-3}]$ (e.g., Japelj et al. 2014; Wang et al. 2015; Gao et al. 2015). Therefore, we set $\epsilon_B \in [10^{-7}, 10^{-2}]$. We find that a reasonable parameter set that can roughly represent the optical and XRT light curves requires $\epsilon_B < 10^{-4}$. We then finalize our fit by setting $\epsilon_B \in [10^{-7}, 10^{-4}]$.

time in their optical afterglow light curves (see Figure 12 of Liang et al. 2013).

Note that the redshift of GRB 110530A is unknown; we set $z = 1$ in our light curve modeling.¹⁴ We also check the dependence of the model parameters on the burst distance by setting $z = 0.5$ and $z = 2.0$. We find that ϵ_e , ϵ_B , n , and q do not change with the redshift. Because of the high uncertainties of t_e , t_s , and θ_j , we also do not find a clear dependence of these parameters on the redshift. However, Γ_0 , $E_{\text{K,iso}}$, and L_0 increase as z increases.

5. DISCUSSION

5.1. Baryonic or Magnetized Jet?

The issue that GRB jets are either baryonic or magnetized is under debate (e.g., Zhang 2011). The GRB radiative efficiency, which is defined as $\eta_\gamma = E_{\gamma,\text{iso}}/(E_{\gamma,\text{iso}} + E_{\text{K,iso}})$, is an essential quantity to understanding the nature of the bursts (e.g., Zhang et al. 2006). The standard internal shock models predict a GRB efficiency of $\sim 1\%$ (Kumar 1999; Panaitescu et al. 1999). E_{K} is the kinetic energy of the fireball that produces the observed gamma-ray energy, and it is estimated at the fireball deceleration time. Assuming that the early optical bump is due to the fireball deceleration by the ambient medium, one then can derive the E_{K} of the fireball at the deceleration time (t_{dec}) by eliminating the possible late energy injection. In this analysis, we obtain $E_{\text{K,iso}} = (2.28 \pm 0.27) \times 10^{53} \text{ erg}$. The corrected gamma-ray energy in the 1–10⁴ keV band is $E_{\gamma,\text{iso}}^c = 1.92 \times 10^{51} \text{ erg}$. Therefore, the internal shock radiation efficiency of GRB 110530A is 0.83%. The total energy injection from 2390/(1+z) to 2997/(1+z) s derived from our model fit is $\sim 3.39 \times 10^{52} \text{ erg}$. Including the delayed energy injection, the efficiency is $\eta = 0.73\%$. This is also consistent with the prediction of the internal shock models. Zhang et al. (2007b) found that some bursts have low efficiency throughout, and these GRBs usually have an X-ray afterglow light curve that smoothly joins the prompt emission light curve without a distinct steep-decay component or an extended shallow-decay component. Fan and Piran (2006) suggested that gamma-ray efficiency is moderate and does not challenge the standard internal shock model. GRB 110530A is consistent with the GRB reported by Zhang et al. (2007b). The low efficiency well agrees with the prediction of the standard internal shock models, implying that the outflow for the prompt emission could be baryonic.

The jet composition in the afterglow phase is also of interest. The ϵ_B value derived from our model fit is much smaller than the typical value reported in literature. For a constant-density medium, the cooling frequency of synchrotron emission is given by $\nu_c = 6.3 \times 10^{15} \text{ Hz} (1+z)^{-1/2} (1+Y)^{-2} \epsilon_{B,-2}^{-3/2} E_{\text{K,iso}}^{-1/2} 52 n^{-1} t_d^{-1/2}$ (Sari et al. 1998; Yost et al. 2003), where Y is the inverse Compton scattering parameter and t_d is the observer's time in days. One can see ν_c is sensitive to ϵ_B . As time increases, ν_c decreases. The extremely low ϵ_B ensures that both the optical and X-ray emissions are still in the regime

¹⁴ Liang et al. (2015) found a close correlation between $L_{\gamma,\text{iso}}$, Γ_0 , and E_p in the burst frame, i.e., $\log L_{\gamma,\text{iso}}/10^{52} \text{ erg s}^{-1} = (-6.38 \pm 0.35) + (1.34 \pm 0.14) \times \log(E_p(1+z)) + (1.32 \pm 0.19) \times \log \Gamma_0$. By setting $z = 1$ and using $E_p = 45 \text{ keV}$ and $\Gamma_0 = 91$, we get $\log L_{\gamma,\text{iso}}/\text{erg s}^{-1} = 50.82 \pm 0.35$ in the energy band of 1–10⁴ keV, where error is measured only for the systematic error of the relation without considering the observed errors of E_p and Γ_0 since no E_p error is available. This is roughly consistent with the observed luminosity by correcting to the same energy band, i.e., $\log L_{\text{iso,obs}}^c/\text{erg s}^{-1} = 50.45 \pm 0.11$.

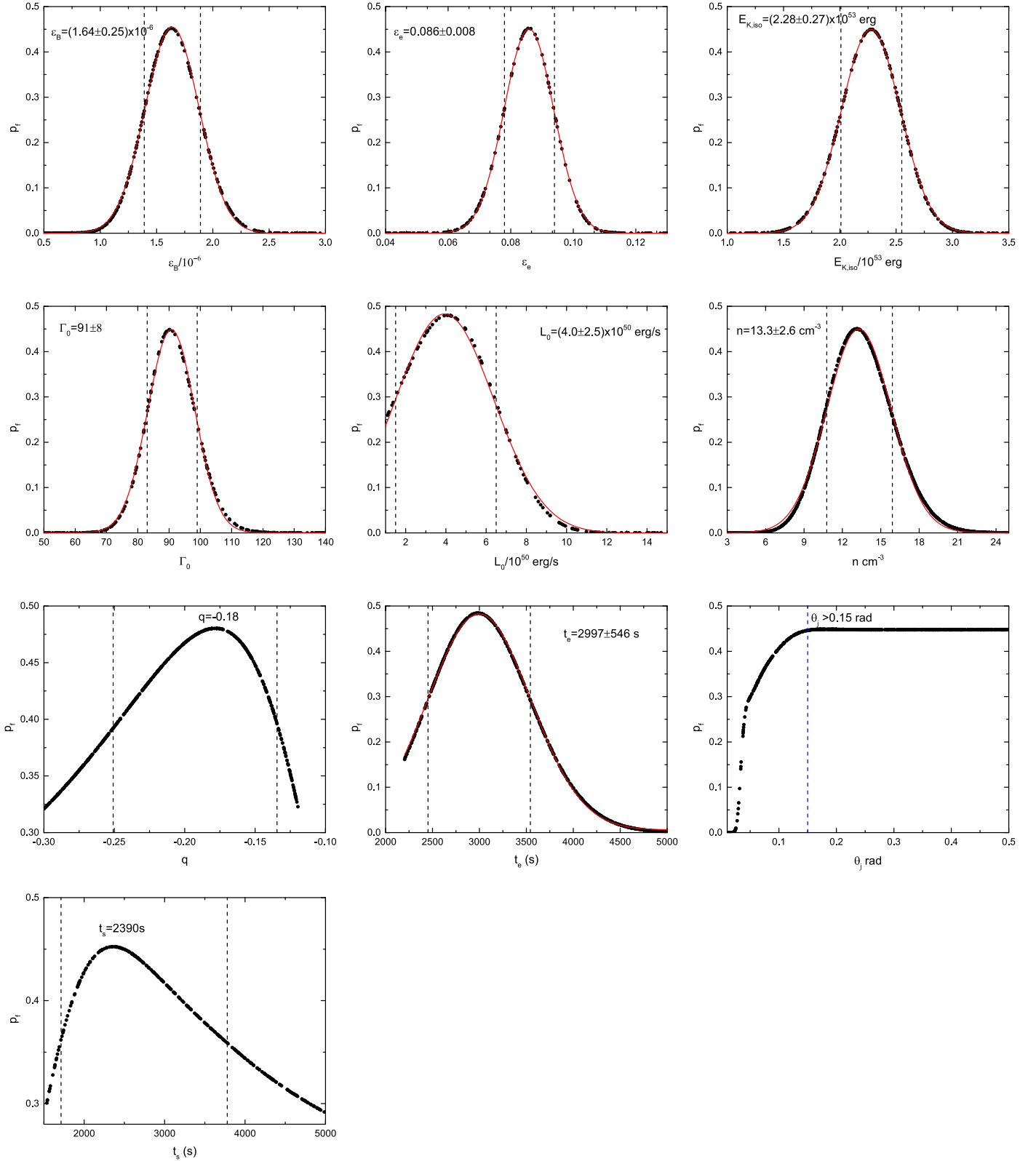


Figure 4. Probability distributions of the forward shock with the delayed energy injection model parameters added along with our Gaussian fits (solid red lines). The dashed black vertical lines mark the 1σ standard deviations. Our fit gives a lower limit on θ_j only.

$\nu < \nu_c$ for several days. The magnetic field strength of the afterglow jet in the co-moving frame is given by $B = (32\pi m_p \epsilon_B n)^{1/2} \Gamma_0 c$, and the power carried by the magnetic field can be derived from $P_B = \pi R_{\text{dec}} c B^2 / 8\pi$, where

$R_{\text{dec}} = 2.25 \times 10^{16} (\Gamma_0/100)^2 (t_{p,z}/100 \text{ s})$ is the deceleration radius of the fireball, m_p is the proton mass, and c is the speed of light. We obtain $B = 0.165 \text{ G}$ and $P_B \sim 5.55 \times 10^{44} \text{ erg s}^{-1}$ for GRB 110530A. Assuming that the electron energy is fully

radiated and the X-ray luminosity is a good representative of the bolometric afterglow luminosity, we estimate the kinetic power of the afterglow jet at the deceleration time with $L_K = L_X(1 - \cos \theta_j)/\epsilon_e$, which gives $L_K > 1.33 \times 10^{46} \text{ erg s}^{-1}$. Therefore, the magnetization of the afterglow jet is $\sigma = P_B/L_K < 0.04$, suggesting that the afterglow jet is baryonic. It is also interesting that the derived B and σ are comparable to the typical values of the jets in BL Lacertae objects, which are suggested to be matter dominated (Zhang et al. 2013).

5.2. Possible Sources of the Delayed Energy Injection

A plateau phase is usually observed in XRT light curves (O'Brien et al. 2006; Zhang et al. 2006; Liang et al. 2007) and in about one-third of optical light curves for long-duration GRBs (Li et al. 2012; Liang et al. 2013). Such a feature can be well explained by the long-lasting energy injection from a constant magnetic-dipole-radiation luminosity within the spin-down timescale of a magnetar (Dai & Lu 1998; Zhang & Mészáros 2001; Lü & Zhang 2014). The injection behavior in this scenario is continuous and starts at a very early epoch. With clear detection of the afterglow onset bump, we propose that the energy injection could have happened after the deceleration of the fireball. In addition, as shown above, the jet in the prompt gamma-ray phase and afterglow phase seems to be matter dominated. These results seem to preclude a scenario of pulsar wind injection.¹⁵ We suggest that the injection may have been caused by a slower shell that is ejected at the same epoch as that of the shells for producing the prompt gamma-rays (Zhang & Mészáros 2002) or delayed ejecta from late accretion activity (Geng et al. 2013). The time delay of the rear shells/ejecta for catching up with the decelerated fireball may have resulted in the delayed energy injection. On the other hand, the energy transfer time from the fireball ejecta to the ambient medium typically extends to thousands of seconds, which may also broaden the onset peak in the thin shell case (Kobayashi & Zhang 2007).

In the scenario of a black hole accretion system, the energy flow from the fall-back accretion may be delayed for a fall-back time t_{fb} and produce giant bumps in the optical bands (Geng et al. 2013). In this scenario, one may place some constraint on the progenitor stars. The radius of the fall-back material can be estimated with $R_{\text{fb}} \sim 6.85 \times 10^{10} \text{ cm} (M_{\text{BH}}/3M_{\odot})^{1/3} (t_{\text{fb}}/10^3 \text{ s})^{2/3}$. We estimate the minimum and maximum radii of the fall-back material with t_s and t_e in the burst frame and have $R_{\text{fb,min}} \sim 7.71 \times 10^{10} \text{ cm} (M_{\text{BH}}/3M_{\odot})^{1/3}$ and $R_{\text{fb,max}} \sim 8.98 \times 10^{10} \text{ cm} (M_{\text{BH}}/3M_{\odot})^{1/3}$. Woosley & Weaver (1995) derived the mass density profile as a function of the radius R with simulations for a pre-supernova star with mass of $25M_{\odot}$ (see also Janiuk & Proga 2008), as shown in Figure 5. The mass density of the shell $R \in [R_{\text{fb,min}}, R_{\text{fb,max}}]$ is about $1.7 \times 10^{-2} \text{ g cm}^{-3}$, and the mass in this shell is $9.62 \times 10^{-3} M_{\odot}$ (corresponding to an energy of $1.71 \times 10^{52} \text{ erg}$), assuming that $M_{\text{BH}} = 3M_{\odot}$. The total energy injection from 2390 to 2997 s derived from our model fit is $\sim 3.39 \times 10^{52} \text{ erg}$, corresponding to a geometrically corrected injection energy of $3.81 \times 10^{50} \text{ erg}$ by taking $\theta_j = 0.15 \text{ rad}$. The jet

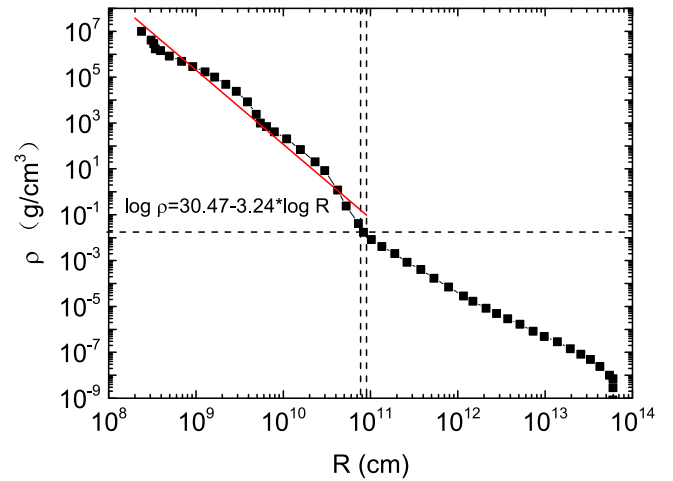


Figure 5. Mass density profile as a function of radius R derived from simulations for a pre-supernova star with mass of $25M_{\odot}$ (Woosley & Weaver 1995). The vertical and horizontal *dashed lines* mark the radii and the corresponding density of fall-back materials for feeding the late accretion in this analysis. The *solid red line* is the power-law fit to the density profile for $R < 9 \times 10^{10} \text{ cm}$.

radiation is only a small fraction (2.23%) of the fall-back mass. Simplifying the mass density profile as a power-law function, $\log \rho/\text{g cm}^{-3} = 30.47 - 3.24 \log R/\text{cm}$ within $R < R_{\text{fb,max}}$, as shown in Figure 5, yields a mass within $R < R_{\text{fb,max}}$ of $\sim 7.5M_{\odot}$. If all the mass within $R < R_{\text{fb,max}}$ is collapsed to form a newly born black hole and its accretion disk, the total collapsed/fall-back mass is about a fraction of 30% of the progenitor star, and the mass in other, outer layers will break out as a supernova.

6. CONCLUSIONS

We have reported our very early optical observations for GRB 110530A and investigated its jet properties together with its X-ray afterglow data. A broad bump with significant flares is observed in the optical light curve at $t < 2000 \text{ s}$, which is followed by a plateau with transition to a normal decaying segment at $t = 3000 \text{ s}$. The X-ray afterglow light curve shows almost the same feature. Our joint spectral fits of the optical and X-ray data show that they are in the same regime, with a photon index of ~ 1.70 . The extinction of the host galaxy is negligible, but the equivalent hydrogen column density of the host galaxy is approximately $1.0 \times 10^{21} \text{ cm}^{-2}$. We model the optical and X-ray light curves with the standard external shock model by considering delayed energy injection and assuming its redshift as 1. Our best parameters derived from an MCMC approach are $\Gamma_0 = 91 \pm 8$, $\epsilon_e = 0.086 \pm 0.008$, $\epsilon_B = (1.64 \pm 0.25) \times 10^{-6}$, $n = 13.3 \pm 2.6 \text{ cm}^{-3}$, $E_{\text{K,iso}} = (2.28 \pm 0.27) \times 10^{53} \text{ erg}$, and $\theta_j \sim 0.15 \text{ rad}$. The energy injection can be described as $L_{\text{in}}/10^{50} \text{ erg s}^{-1} = (4.0 \pm 2.5) \times t^{-0.18}$, which starts at $\sim 2390 \text{ s}$ and lasts only about 700 s. Based on our modeling results, the radiative efficiency of the GRB fireball is $\sim 1\%$, and the magnetic field strength and the magnetization parameter of the afterglow jet are $B = 0.165 \text{ G}$ and $\sigma < 0.04$, respectively. We propose that the jet is matter dominated, and discuss possible sources of the delayed energy injection.

The most striking observation of GRB 110530A is its early broad bump followed by a plateau in its R band afterglow light curve. We have shown that the standard forward shock model

¹⁵ It was also proposed that the magnetic-dipole-radiation luminosity of a magnetar can dramatically increase with time, which may lead to a significant bump in the afterglow light curves, if the magnetar is spun up by the accretion matter (Dai & Liu 2012). In this scenario, energy injection is not significant in the early epoch and may feature as delayed energy injection in the late epoch.

with a delayed injection can roughly fit the global feature of the light curves. We address the flickerings in the optical and X-ray light curves as superimposed flares that may have internal origins. We should note that these flickerings, especially the significant flickering at around 3000 s in the X-ray band, may also be due to the delayed energy injection. Zhang & Mészáros (2001) analyzed the energy injection and corresponding signature that could show up in afterglow light curves. They showed that injection by a Poynting-flux-dominated shell that has an energy comparable to that of the initial fireball would lead to a gradual achromatic bump. In the case where the injection is kinetic-energy-dominated, the results depend on the situation of the collision between the injected (rear) shells and initial (leading) shells. If the collision is mild, the signature shown in the light curves may be analogous to that in the Poynting-flux-dominated injection case. In a violent collision a significant flare-like bump may be observed (see Figure 5 of Zhang & Mészáros 2001). If the delayed energy injection is fed by the fall-back materials, the delayed energy will also cause a notable rise of the Lorentz factor of the external shock, which will generate a bump in the multiple-band afterglows, as seen in GRB 081029 and GRB 100621A (Nardini et al. 2011; Geng et al. 2013; Greiner et al. 2013).

This work is supported by the National Basic Research Program of China (973 Program, Grant No. 2014CB845800), the National Natural Science Foundation of China (Grant No. 11533003, 11103036, U1331202, U1231115, and U1331101), the Strategic Priority Research Program “The Emergence of Cosmological Structures” of the Chinese Academy of Sciences (Grant XDB09000000), and the Guangxi Science Foundation (Grant No. 2013GXNSFFA019001). We also acknowledge our use of public data from the Swift data archive.

REFERENCES

- Abdo, A. A., Ackermann, M., Arimoto, M., et al. 2009, *Sci*, **323**, 1688
- Band, D., Matteson, J., Ford, L., et al. 1993, *ApJ*, **413**, 281
- Bardho, O., Gendre, B., Rossi, A., et al. 2016, arXiv:1602.09014
- Beloborodov, A. M. 2010, *MNRAS*, **407**, 1033
- Burrows, D. N., Hill, J. E., Nousek, J. A., et al. 2005a, *SSRv*, **120**, 165
- Burrows, D. N., Romano, P., Falcone, A., et al. 2005b, *Sci*, **309**, 1833
- Colgate, S. A. 1974, *ApJ*, **187**, 333
- Cucchiara, A., Cenko, S. B., Bloom, J. S., et al. 2011, *ApJ*, **743**, 154
- Dai, Z. G., & Liu, R.-Y. 2012, *ApJ*, **759**, 58
- Dai, Z. G., & Lu, T. 1998, *A&A*, **333**, L87
- Dai, Z. G., Wang, X. Y., Wu, X. F., & Zhang, B. 2006, *Sci*, **311**, 1127
- D’Avanzo, P. 2011a, GCN, **12058**, 1
- D’Avanzo, P., Barthelmy, S. D., Beardmore, A. P., et al. 2011b, GCN, **12046**, 1
- De Cia, A., Vreeswijk, P., Xu, D., Telting, J., & Jakobsson, P. 2011, GCN, **12054**, 1
- Eichler, D., Livio, M., Piran, T., & Schramm, D. N. 1989, *Natur*, **340**, 126
- Evans, P. A., Beardmore, A. P., Page, K. L., et al. 2009, *MNRAS*, **397**, 1177
- Fan, Y., & Piran, T. 2006, *MNRAS*, **369**, 197
- Fan, Y. Z., & Wei, D. M. 2005, *MNRAS*, **364**, L42
- Gao, H., Lei, W.-H., Zou, Y.-C., Wu, X.-F., & Zhang, B. 2013, *NAR*, **57**, 141
- Gao, H., Wang, X.-G., Mészáros, P., & Zhang, B. 2015, *ApJ*, **810**, 160
- Gehrels, N., Chincarini, G., Giommi, P., et al. 2004, *ApJ*, **611**, 1005
- Gehrels, N., Ramirez-Ruiz, E., & Fox, D. B. 2009, *ARA&A*, **47**, 567
- Geng, J. J., Wu, X. F., Huang, Y. F., & Yu, Y. B. 2013, *ApJ*, **779**, 28
- Giannios, D. 2008, *A&A*, **480**, 305
- Greiner, J., Krühler, T., Nardini, M., et al. 2013, *A&A*, **560**, A70
- Huang, Y. F., Dai, Z. G., & Lu, T. 1999, *MNRAS*, **309**, 513
- Ioka, K. 2010, in AIP Conf. Proc. 1279, Deciphering the Ancient Universe with Gamma-ray Bursts, ed. N. Kawai & S. Nagasaki (Melville, NY: AIP), 28
- Janiuk, A., & Proga, D. 2008, *ApJ*, **675**, 519
- Japelj, J., Kopač, D., Kobayashi, S., et al. 2014, *ApJ*, **785**, 84
- Jordi, K., Grebel, E. K., & Ammon, K. 2006, *A&A*, **460**, 339
- Kann, D. A., Klose, S., Zhang, B., et al. 2010, *ApJ*, **720**, 1513
- Kobayashi, S., & Zhang, B. 2007, *ApJ*, **655**, 973
- Kumar, P. 1999, *ApJL*, **523**, L113
- Kumar, P., & Zhang, B. 2015, *PhR*, **561**, 1
- Li, L., Liang, E.-W., Tang, Q.-W., et al. 2012, *ApJ*, **758**, 27
- Liang, E. W., Dai, Z. G., & Wu, X. F. 2004, *ApJL*, **606**, L29
- Liang, E.-W., Li, L., Gao, H., et al. 2013, *ApJ*, **774**, 13
- Liang, E.-W., Lin, T.-T., Lü, J., et al. 2015, *ApJ*, **813**, 116
- Liang, E.-W., Yi, S.-X., Zhang, J., et al. 2010, *ApJ*, **725**, 2209
- Liang, E. W., Zhang, B., O’Brien, P. T., et al. 2006, *ApJ*, **646**, 351
- Liang, E.-W., Zhang, B.-B., & Zhang, B. 2007, *ApJ*, **670**, 565
- Lü, H.-J., & Zhang, B. 2014, *ApJ*, **785**, 74
- Lyu, F., Liang, E.-W., Liang, Y.-F., et al. 2014, *ApJ*, **793**, 36
- MacFadyen, A. I., & Woosley, S. E. 1999, *ApJ*, **524**, 262
- Marshall, F. E., & D’Avanzo, P. 2011, GCN, **12057**, 1
- Mészáros, P. 2002, *ARA&A*, **40**, 137
- Mészáros, P. 2006, *RPPH*, **69**, 2259
- Mészáros, P., & Rees, M. J. 1993, *ApJ*, **405**, 278
- Mészáros, P., & Rees, M. J. 1997, *ApJ*, **476**, 232
- Narayan, R., Paczynski, B., & Piran, T. 1992, *ApJL*, **395**, L83
- Nardini, M., Greiner, J., Krühler, T., et al. 2011, *A&A*, **531**, A39
- Nousek, J. A., Kouveliotou, C., Grupe, D., et al. 2006, *ApJ*, **642**, 389
- O’Brien, P. T., Willingale, R., Osborne, J., et al. 2006, *ApJ*, **647**, 1213
- Paczynski, B. 1986, *ApJL*, **308**, L43
- Panaitelescu, A., & Kumar, P. 2001, *ApJL*, **560**, L49
- Panaitelescu, A., Spada, M., & Mészáros, P. 1999, *ApJL*, **522**, L105
- Perley, D. A., Bloom, J. S., Klein, C. R., et al. 2010, *MNRAS*, **406**, 2473
- Piran, T. 2004, *RvMP*, **76**, 1143
- Preece, R. D., Briggs, M. S., Malozzi, R. S., et al. 2000, *ApJS*, **126**, 19
- Rees, M. J., & Meszaros, P. 1992, *MNRAS*, **258**, 41
- Rees, M. J., & Meszaros, P. 1994, *ApJL*, **430**, L93
- Sari, R., & Piran, T. 1999, *ApJ*, **520**, 641
- Sari, R., Piran, T., & Narayan, R. 1998, *ApJL*, **497**, L17
- Schlegel, D. J., Finkbeiner, D. P., & Davis, M. 1998, *ApJ*, **500**, 525
- van Paradijs, J., Groot, P. J., Galama, T., et al. 1997, *Natur*, **386**, 686
- Virgili, F. J., Mundell, C. G., Pal’shin, V., et al. 2013, *ApJ*, **778**, 54
- Volnova, A., Klunko, E., & Pozanenko, A. 2011, GCN, **12062**, 1
- Vurm, I., Beloborodov, A. M., & Poutanen, J. 2011, *ApJ*, **738**, 77
- Wang, X.-G., Zhang, B., Liang, E.-W., et al. 2015, *ApJS*, **219**, 9
- Wijers, R. A. M. J., & Galama, T. J. 1999, *ApJ*, **523**, 177
- Woosley, S. E. 1993, *ApJ*, **405**, 273
- Woosley, S. E., & Bloom, J. S. 2006, *ARA&A*, **44**, 507
- Woosley, S. E., & Weaver, T. A. 1995, *ApJS*, **101**, 181
- Xin, L.-P., Wang, Y.-Z., Lin, T.-T., et al. 2016, *ApJ*, **817**, 152
- Xin, L. P., Zheng, W. K., Wang, J., et al. 2010, *MNRAS*, **401**, 2005
- Yost, S. A., Harrison, F. A., Sari, R., & Frail, D. A. 2003, *ApJ*, **597**, 459
- Zhang, B. 2011, *CRPhy*, **12**, 206
- Zhang, B., Fan, Y. Z., Dyks, J., et al. 2006, *ApJ*, **642**, 354
- Zhang, B., & Mészáros, P. 2001, *ApJL*, **552**, L35
- Zhang, B., & Mészáros, P. 2002, *ApJ*, **566**, 712
- Zhang, B., & Mészáros, P. 2004, *IJMPA*, **19**, 2385
- Zhang, B., & Pe’er, A. 2009, *ApJL*, **700**, L65
- Zhang, B., & Yan, H. 2011, *ApJ*, **726**, 90
- Zhang, B., Zhang, B.-B., Liang, E.-W., et al. 2007a, *ApJL*, **655**, L25
- Zhang, B.-B., Liang, E.-W., & Zhang, B. 2007b, *ApJ*, **666**, 1002
- Zhang, B.-B., Zhang, B., Liang, E.-W., et al. 2011, *ApJ*, **730**, 141
- Zhang, J., Liang, E.-W., Sun, X.-N., et al. 2013, *ApJL*, **774**, L5
- Zhang, W., Woosley, S. E., & MacFadyen, A. I. 2003, *ApJ*, **586**, 356
- Zheng, W.-K., Deng, J.-S., Zhai, M., et al. 2008, *ChJAA*, **8**, 693